

Sulfurized Polyacrylonitrile Cathodes with High Compatibility in Both Ether and Carbonate Electrolytes for Ultrastable Lithium–Sulfur Batteries

Xiaofei Wang, Yumin Qian, Lina Wang,* Hao Yang, Huilan Li, Yu Zhao,* and Tianxi Liu*

Sulfurized polyacrylonitrile (SPAN) is a promising material capable of suppressing polysulfide dissolution in lithium–sulfur (Li–S) batteries with carbonate electrolyte. However, undesirable spontaneous formation of soluble polysulfides may arise in the ether electrolyte, and the conversion of sulfur in SPAN during the lithiation/delithiation processes is yet to be understood. Here, a highly reliable Li–S system using a freestanding fibrous SPAN cathode, as well as the sulfur conversion mechanism involved, is demonstrated. The SPAN shows high compatibility in both ether and carbonate electrolytes. The sulfur atoms existing in the form of short $-S_2-$ and $-S_3-$ chains are covalently bonded to the pyrolyzed PAN backbone. The electrochemical reduction of the SPAN by Li^+ is a single-phase solid–solid reaction with Li_2S as the sole discharge product. Meanwhile, the parasitic reaction between Li^+ and $C=N$ bonds exists upon the first discharge, and the residual Li^+ enhances the conductivity of the backbone. The recharge ability and rate capability are kinetically dominated by the activation of Li_2S nanoflakes generated during discharge. At 800 mA g^{-1} , a specific capacity of 1180 mAh g^{-1} is realized without capacity fading in the measured 1000 cycles, which makes SPAN promising for practical application.

soluble intermediate products of lithium polysulfides (Li_2S_n , $2 < n \leq 8$), however, result in internal shuttle of the cell as well as undesirable parasitic reactions with the Li anode.^[2] Besides, the cathode suffers from a 70–80% volume expansion when sulfur is finally reduced to Li_2S ,^[3] and the electrical insulating nature of S_8 ($5 \times 10^{-30}\text{ S cm}^{-1}$) and Li_2S ($10^{-13}\text{ S cm}^{-1}$)^[4] requires the addition of a large amount of conductive carbons which consequently reduce the realistic energy density.^[5] Up to now, considerable efforts have been made to prevent the diffusion and nonelectrochemical reactions of Li_2S_n . Several strategies have been proposed to retain the sulfur in the cathode matrix, such as physical trapping of Li_2S_n within porous carbons^[6] and chemical interactions of Li_2S_n with polar molecules (e.g., metal oxides,^[7] metal sulfides,^[8] etc.). As a matter of fact, it is still hard to overcome the electromigration of S_n^{2-} anions driven by the electrical field.

1. Introduction

Lithium–sulfur (Li–S) battery technology is attractive because of the low cost and abundance of elemental sulfur (S_8), and very high specific capacity of 1675 mAh g^{-1} by complete reduction of cycloocta S_8 to lithium sulfide (Li_2S).^[1] The highly

One plausible approach is to confine the small sulfur allotropes (S_{2-4}) within nanoporous carbon with pore size of $\approx 0.5\text{ nm}$ upon heating.^[9] In this case, the unfavorable transition from S_8 to S_4^{2-} at $\approx 2.3\text{ V}$ (vs Li/Li^+) is avoided and the cell typically gives a single plateau at $\approx 1.9\text{ V}$ (vs Li/Li^+). Another promising approach is to trap the S atoms in polymer backbones via chemical bonding like $C-S$ or $C=S$. The latter approach has been extensively investigated since the first demonstration by taking advantage of the well-known cyclization chemistry of polyacrylonitrile (PAN).^[10] The mechanism is yet to be further clarified. The synthesis with excess S_8 at a temperature $\geq 300\text{ }^\circ\text{C}$ in the absence of O_2 is assumed to be a sulfur-assisted dehydrocyclization process, yielding a sulfurized polyacrylonitrile (SPAN). Spectroscopic characterizations identified that sulfur is present in the form of $-S_x-$ ($0 < x < 8$) chains covalently bonding to the cyclized and dehydrogenated PAN backbones through $C-S$ bonds.^[11] The SPAN features a single sloped voltage plateau at $\approx 1.9\text{ V}$ (vs Li/Li^+) in carbonate electrolyte, which is widely used in current state-of-the-art Li-ion batteries. Because of the strong nucleophilic reactivity between Li_2S_n and carbonate solvents, conventional Li–S cells with S_8 cathodes are widely prepared from a mixture of 1,3-dioxolane (DOL)/dimethoxyethane (DME)-based ether electrolyte.^[12] As a result, it is generally believed that SPAN completely avoids

X. Wang, Prof. L. Wang, H. Yang, H. Li, Prof. T. Liu
State Key Laboratory for Modification of Chemical Fibers
and Polymer Materials
College of Materials Science and Engineering
Innovation Center for Textile Science and Technology
Donghua University
Shanghai 201620, China
E-mail: linawang@dhu.edu.cn; txliu@dhu.edu.cn

Dr. Y. Qian, Prof. Y. Zhao
Institute of Functional Nano and Soft Materials (FUNSOM)
Jiangsu Key Laboratory for Carbon-Based Functional Materials
and Devices
Soochow University
Jiangsu 215123, China
E-mail: yuzhao@suda.edu.cn

 The ORCID identification number(s) for the author(s) of this article can be found under <https://doi.org/10.1002/adfm.201902929>.

DOI: 10.1002/adfm.201902929

the dissolution and the resulting redox shuttle effect of Li_2S_n in carbonate electrolyte. When using the ether electrolyte in Li–S cells with SPAN cathodes, the electrochemical characteristics are contradictory, as verified by the upper voltage plateau at ≈ 2.3 V (vs Li/Li⁺) and the fast capacity fading.^[11b,e,13] Such an unusual phenomenon was attributed to the spontaneous formation of high-order Li_2S_n and S_8 upon recharge, resulted from the high solubility of Li_2S_n in ether solvents.^[11b,13b] Nonetheless, the molecular structures of SPAN, the structure–property relationship, and the reaction mechanism during lithiation/delithiation processes have not yet been well established. In review of published results, the structural and electrochemical characteristics of SPAN are strongly correlated to the synthetic conditions.^[11] Despite the ease of preparation, SPAN electrodes with a long shelf life and a high energy density are still in urgent need because the saturated sulfur content in SPAN of ≈ 40 wt%. The routine fabrication of electrodes with the introduction of electrochemically inactive carbon additives, polymer binders, and metallic current collectors further significantly reduce the overall gravimetric capacity of the cell.

Herein, we demonstrate an ultrastable Li–S system with flexible and freestanding SPAN cathodes, which are composed of conductive 3D network of electrospun SPAN nanofibers incorporated with an appropriate amount of carbon nanotubes (CNTs). Such an electrode architecture benefits fast charge transport and accommodation of volume expansion/reconversion during lithiation/delithiation processes. We further demonstrate that the strong interaction between π -conjugated pyrolyzed PAN backbone and the covalently bonded short $-\text{S}_x-$ ($x = 2, 3$) chains enabling highly reversible redox reactions in both ether and carbonate electrolytes. The S atoms bonding two adjacent carbon atoms on the side of hexatomic ring should be responsible for the absence of soluble Li_2S_n in ether electrolyte. The electrochemical reduction of SPAN by Li⁺ is a single-phase solid–solid reaction with Li_2S as the sole sulfide product. An extra parasitic reaction between Li⁺ and C=N bonds makes the backbone more conductive.

2. Results and Discussion

2.1. Preparation and Characterization of SPAN/CNT Nanofibers

As illustrated in Figure 1a, the overall synthetic procedure of SPAN/CNT involves a simple electrospinning preparation and subsequent thermal treatment. The electrospun PAN/CNT films were produced from N,N-dimethylformamide (DMF) solutions containing PAN and CNTs. Then, the dried precursor films were heated with S_8 under N_2 flow at 350 °C, and maintained at this temperature for 3 h for sulfuration. During the thermal treatment, S_8 cleaved into small chain sulfur species ($-\text{S}_x-$, $x < 8$), and reacted with H atoms to facilitate the dehydrogenation and cyclization of PAN. The two processes occurred simultaneously and promoted each other as proposed in Figure S1 (Supporting Information). It was hypothesized that the $-\text{S}_x-$ fragment was covalently bonded to the C=C bond of PAN backbone to form various structural SPAN polymers. The as-prepared SPAN/CNT texture is robust and flexible and can be readily punched into freestanding, fracture-free electrodes.

The microstructure of the PAN and SPAN films with/without incorporated CNTs is revealed by field-emission scanning electron microscopy (FESEM). The PAN film possesses a nanofibrous-network-like structure, which is constructed from uniformly interconnected long fibers with a mean diameter of ≈ 400 nm (Figure 1b). The nanofibrous network is maintained during sulfuration (Figure 1c). The resultant SPAN exhibits increased diameter of ≈ 500 nm, which should attribute to the infiltrated saturated sulfur species. The average thickness of the flexible and freestanding SPAN film is 40 ± 5 μm (Figure 1d). The incorporation of CNTs into PAN (mass ratio of CNTs to PAN is 12 wt%, denoted as SPAN/CNT-12) roughens the nanofibrous surface (Figure 1e). The size of the nanofibers (Figure 1f) and the overall thickness of SPAN/CNT-12 electrode (Figure 1g) are similar with those of SPAN without CNT incorporation. Similar morphology is observed in other SPAN/CNT films with different amounts of CNTs (Figure S2, Supporting Information). High-resolution transmission electron microscopy (TEM) images show that the CNTs are uniformly dispersed in the nanofibers (Figure 1h). Energy-dispersive X-ray spectroscopy (EDS) analysis shows homogeneous distribution of S, C, and N elements throughout the nanofibers (Figure 1i–k), suggesting that sulfur should be loaded within the polymer matrix rather than aggregated on the surface.

To understand the crystallinity, X-ray diffraction (XRD) characterizations were carried out. As shown in Figure 2a, orthorhombic S_8 exhibits sharp and intense diffraction peaks.^[14] Whereas, no diffraction peaks of crystalline sulfur and crystalline PAN that typically at 16.8° ^[15] are observed in SPAN, suggesting that sulfur is in amorphous phase. The distinct broad peak at 26° corresponds to the graphitic (002) plane,^[8b,11d] arising from the graphitization of PAN during thermal treatment. Raman spectra (Figure 2b) and Fourier transform infrared spectra (FTIR, Figure 2c) were used to analyze the chemical structure of the as-prepared SPAN. Three prominent bands at 176, 296, and 373 cm^{-1} in Raman spectra are observed, which can be assigned to the stretch, bending, and deformation of C–S bonds, respectively.^[11a,e] The bands at 460 and 930 cm^{-1} are from S–S stretch.^[11a,d,e] All of the SPAN materials exhibit D-band (disorder-induced phonon mode) at 1330 cm^{-1} and G-band (graphite band) at 1540 cm^{-1} , suggesting a disordered graphite-like stacking of the polyaromatic layers. The peak at 1458 cm^{-1} corresponds to the C–C and C–S stretch.^[11c] The signals of C–S and S–S bonds at 671, 936, and 511 cm^{-1} in the FTIR spectra can also be clearly assigned,^[11a,d,e,16] providing additional information on the atomic configuration of carbon matrix. The peaks at 1495 and 1359 cm^{-1} are assigned to the C=C and C–C deformation, and the peaks at 1427 and 1235 cm^{-1} correspond to C=N stretch.^[10b,11d,16b] The peak at 802 cm^{-1} indicates the formation of hexahydric rings via the dehydrogenation.^[10b,11a,16] In brief, the signals of C–C, C=C, and C=N confirm the comprehensive sulfur-assisted dehydrogenation, cyclization, and aromatization of the aliphatic PAN to a polyaromatic system.

X-ray photoelectron spectroscopy (XPS) was used to characterize the elemental chemical states of SPAN/CNT-12. Prominent signals of C 1s, N 1s, and S 2p are detected from the XPS survey spectrum (Figure S3a, Supporting Information). The C 1s peak is composed of three contributions (Figure S3b,

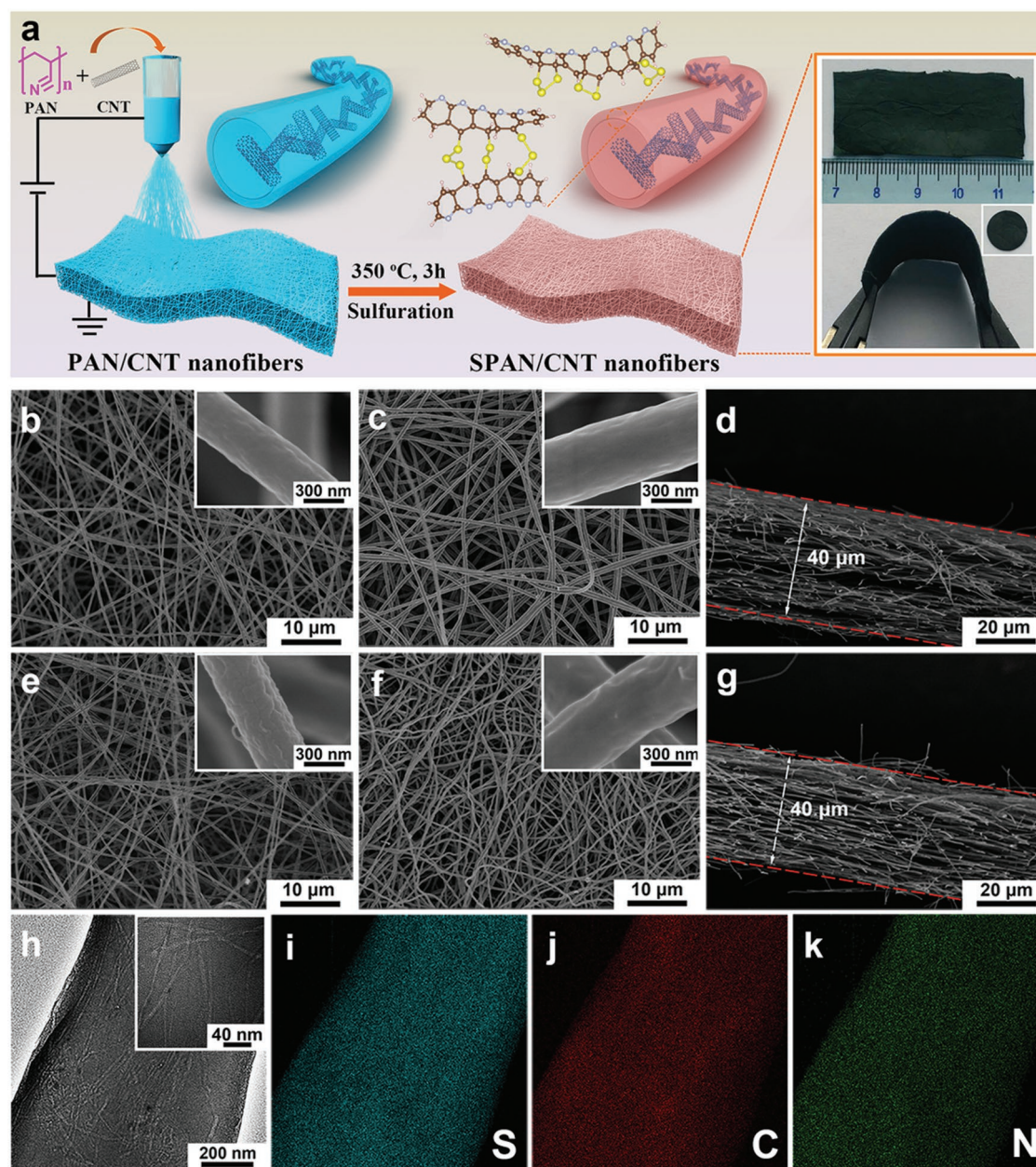


Figure 1. a) Schematic illustration for synthetic procedure of SPAN/CNT electrodes. The inset orange boxes are digital pictures of the flexible and freestanding electrodes. SEM images of b) PAN precursor film, c) SPAN film, e) PAN/CNT-12 precursor film, f) SPAN/CNT-12 film, and d, g) cross-sectional images of SPAN and SPAN/CNT-12 electrodes. h) TEM images of a single SPAN/CNT-12 fiber and i–k) the corresponding elemental mapping of S, C, and N. The inset white boxes are images with high magnifications.

Supporting Information), which is assigned to C–C bond with sp^2 hybridization (284.6 eV), covalent C–S bond formed upon sulfuration (285.2 eV), and sp^2 C=N bond (286.6 eV).^[11a,e,14] In the S 2p spectrum (Figure S3c, Supporting Information), the main peaks at 163.4 eV (S 2p_{3/2}) and 164.6 eV (S 2p_{1/2}) are assigned to the C–S and S–S bonds, respectively.^[11e,14,17] The S 2p_{3/2} peak at 161.7 eV should arise from the adsorbed H₂S.^[11b,14] The N 1s spectrum (Figure S3d, Supporting Information) shows two peaks of pyridinic (C=N–C, 398.2 eV) and pyrrolic nitrogen atoms (C–NH–C, 400.0 eV),^[11f,18] suggesting PAN fibers are cross-linked during the sulfuration.

Moreover, thermal gravimetric analysis (TGA) further confirms the formation of C–S bonds in SPAN nanofibers (Figure 2d). In comparison with S₈ that exhibits a thorough weight loss of 100% in the temperature range of 180–300 °C, the weight loss of SPAN/CNT-12 occurs at much higher temperature over 500 °C, indicating that S atoms are attached to PAN through strong covalent bonding. Combined with XPS and TGA analysis, it is highly possible that short –S_x– chains should be covalently bonded to the positively polarized carbon atoms in the hexatomic ring through S–C bonds, either between two adjacent hexatomic rings or on one side of the hexatomic ring.

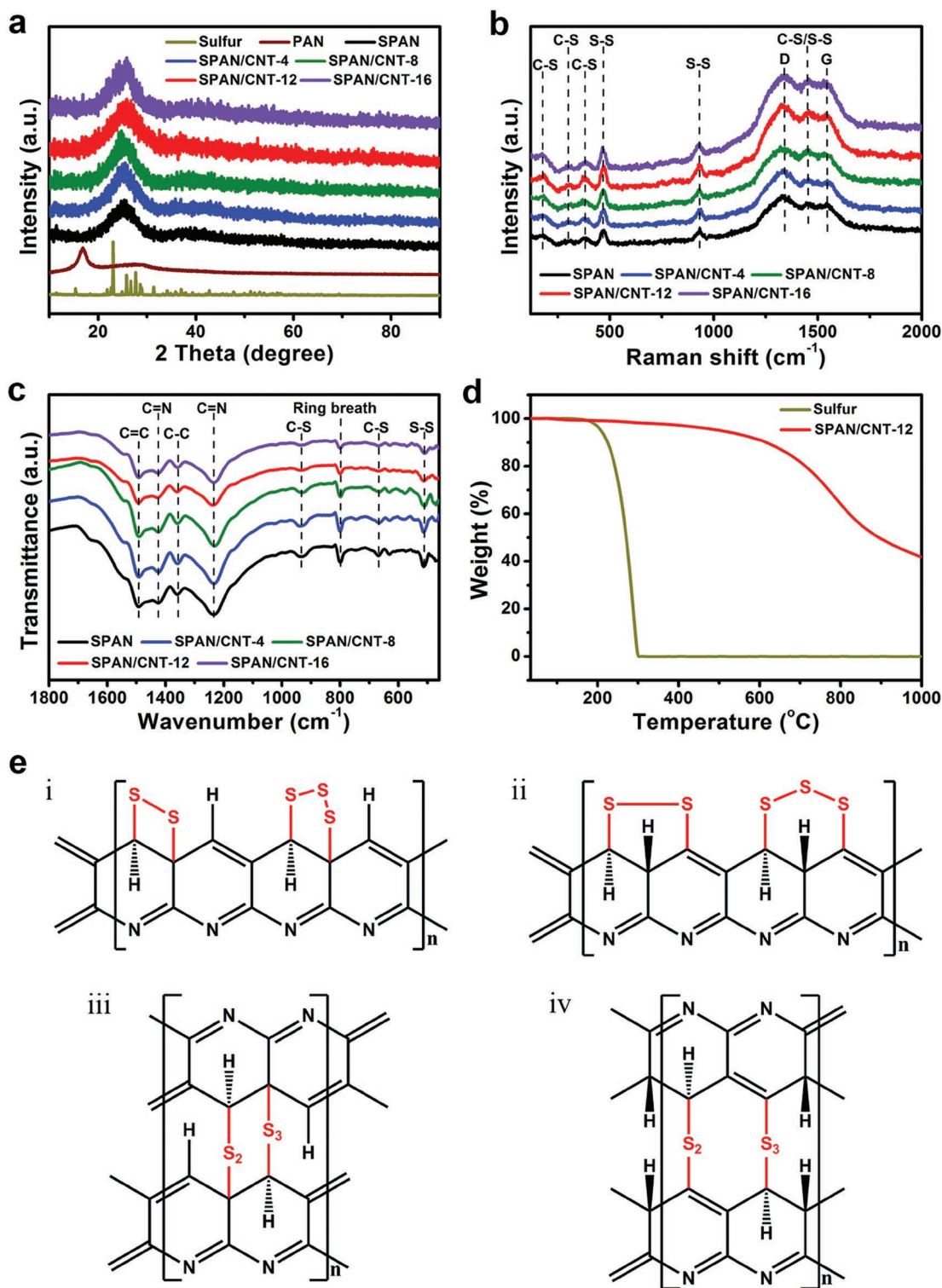


Figure 2. a) XRD patterns of sulfur (S_8), PAN, SPAN, and SPAN/CNT composites with various contents of CNT. b) Raman spectra and c) FTIR spectra of SPAN and SPAN/CNT composites. d) TGA profiles of S_8 and SPAN/CNT-12 from ambient to 1000 °C at 20 °C min⁻¹ in N₂ atmosphere. e) Proposed chemical structures of SPAN.

The element content analysis (Table S1, Supporting Information) offers more information on identification of the chemical structure of SPAN. The sulfur content in bare SPAN is saturated

at 42.8 wt%, which is decreased by 2 wt% in SPAN/CNT composites. The result suggests the introduction of CNTs does not obstruct the deep interaction between nanofibrous PAN and

sulfur. The SPAN shows a higher atomic C/N ratio (3.11) than PAN (3.02), indicating the slight denitrogenation of PAN.^[13b] The C/H ratio increases dramatically from 0.85 of PAN to 3.94 of SPAN as a result of severe dehydrogenation and sulfuration of PAN during thermal treatment. It should note that complete removal of H is difficult, with 0.86 wt% H remaining in SPAN. The C/H ratio of SPAN/CNT-12 is increased to 4.74, which should be due to the incorporation of CNTs rather than graphitization of PAN. The sum molecular formula of SPAN is thus determined to be $C_4N_{1.3}HS_{1.6}$, indicating every 5 C atoms contain ≈ 2 S atoms. Due to the higher dissociation energy of the C–S (272 kJ mol^{-1}) bond than that of the S–S bond (251 kJ mol^{-1}),^[11d] the ideal $-S_x-$ in a stable SPAN should be with $x \leq 3$ based on the ratio of C to S. If taking the trace amount of residual H into consideration, four possible chemical structures of SPAN are proposed in Figure 2e, in which 80% of S atoms covalently bond to C, and the other 20% form $-C-S-S-S-C-$ chains.

2.2. Electrochemical Characteristics of SPAN/CNT Nanofibers

DOL/DME containing 1 M lithium bis(trifluoromethanesulfone) imide (LiTFSI) and 0.2 M $LiNO_3$ was first employed as the electrolyte to assess the electrochemical performance of the SPAN and SPAN/CNT cathodes. As shown in the galvanostatic discharge–charge profiles at a current density of 200 mA g^{-1} (Figure 3a,b), both SPAN and SPAN/CNT-12 feature a single long output plateau at low discharge potential of 1.4 and 1.6 V (vs Li/Li^+) but a high initial specific discharge capacity of 1767 and 1884 mAh g^{-1} , respectively. Both electrodes show large irreversible capacity loss upon the first recharge. In subsequent cycles, the reaction kinetics is improved as evident by the gradually decreased voltage hysteresis, enlarged reversible capacity, and nearly 100% Coulombic efficiency (CE). Besides, the decreased interfacial charge transfer resistance (R_{inf}) of cycled cells also suggests the reaction kinetics is accelerated through activation and stabilization of electrochemical active species (Figure 3c). Compared with SPAN, SPAN/CNT-12 displays smaller voltage hysteresis and higher reversible capacity, which should result from higher electronic conductivity and faster ionic diffusion by CNT incorporation, as verified by the lower R_{inf} of both fresh and cycled cells with SPAN/CNT-12.

In accordance with the single voltage plateaus at 2.1 V in galvanostatic profiles, the SPAN/CNT-12 cathode exhibits one pair anodic/cathodic peaks in the cyclic voltammetry (CV) curves (Figure S4, Supporting Information). In contrast, S_8 cathode exhibits two pairs of voltage plateaus at ≈ 2.3 and 2.1 V, which are generally accepted as the solid–liquid phase transition from S_8 to Li_2S_4 and a liquid–solid transition from Li_2S_4 to Li_2S , respectively.^[6a,c,7b] The vanishing of the voltage plateau at 2.3 V implies the elimination of high-order Li_2S_n , beyond Li_2S_4 at least. The 100% capacity retention and 100% CE of these SPAN and SPAN/CNT-12 electrodes after a few activation cycles strongly support the absence of soluble Li_2S_n (Figure S5a, Supporting Information). The specific capacity increases considerably with increasing CNT contents. A reversible capacity of $\approx 1400 \text{ mAh g}^{-1}$ retains over 200 cycles at 200 mA g^{-1} with SPAN/CNT-12 (Figure S5b, Supporting Information). However, further increase would result in the agglomeration of CNTs in

nanofibers, which prevents the electrode from achieving high capacity (Figure S6, Supporting Information). The rate performance of SPAN/CNT-12 is presented in Figure 3d. A reversible capacity of 885 mAh g^{-1} is achieved at a current density of 1600 mA g^{-1} (Figure 3e). At a moderate current density of 800 mA g^{-1} , highly overlapped steady-state voltage profiles (Figure 3f) with a specific capacity of 1180 mAh g^{-1} are achieved in the measured 800 cycles with nearly 100% CE (Figure 3g). The corresponding capacity based on the total cathode mass is $484 \text{ mAh g}^{-1}_{\text{cathode}}$. Such an overall electrochemical performance is superior to most SPAN-based materials (Table S2, Supporting Information). It should be mentioned that conventional SPAN cathodes usually contain additional conductive carbon additives (10–20 wt%) and polymer binder (10–15 wt%), which in fact leads to a low sulfur loading in the final electrodes (22–39 wt%).^[10,11,13–15,19]

The controlled electrolyte volume to active sulfur mass ratio, as generally presented as E/S, is $30 \mu\text{L mg}^{-1}$ in this study. The specific capacity of SPAN/CNT-12 increases considerably with increasing the E/S ratio from 10 to $30 \mu\text{L mg}^{-1}$, whereas further increased E/S ratio does not certainly bring a higher capacity (Figure S7, Supporting Information). The energy density is 1016 Wh kg^{-1} based on the cathode mass at a current density of 800 mA g^{-1} . If taking the weight of anode, separator, and electrolyte into consideration, the overall battery energy density is $\approx 62 \text{ Wh kg}^{-1}$ (Table S3, Supporting Information). The value is still lower compared with that of state-of-the-art Li-ion batteries mainly due to a higher electrolyte intake, which holds the promise to be reduced by adjusting the porosity of the SPAN/CNT electrodes. The optimized E/S ratio is slightly higher than those of the sulfur electrodes prepared from the traditional slurry-casting method ($10\text{--}25 \mu\text{L mg}^{-1}$) with a similar sulfur loading, as illustrated in Table S4 (Supporting Information). Nonetheless, the significantly improved electrochemical performance has compensated the sacrificial battery energy density to some extent. We further used electrodes with higher sulfur loading through a layer-by-layer configuration^[20] to evaluate the electrochemical performance of SPAN/CNT-12. The electrochemical performance of the double-layered electrode (typical sulfur loading of $\approx 4.0 \text{ mg cm}^{-2}$) does not show obvious performance decay as the increase of sulfur loading. The reversible capacity achieved at 800 mA g^{-1} reaches 1100 mAh g^{-1} (Figure S8a,b, Supporting Information), which is similar with those achieved in SPAN/CNT-12 with lower sulfur loading. Besides, the reversible capacity is well maintained over 810 mAh g^{-1} at a higher current rate of 1600 mA g^{-1} (Figure S8c,d, Supporting Information), demonstrating the advantages of SPAN/CNT-12 for Li–S batteries with high areal capacity.

2.3. The Structure–Property Relationship of SPAN

The as-prepared SPAN electrodes show good compatibility in ether-based electrolytes. This assessment is of utmost importance because it allows the correlation of electrochemical performance with chemical structures of SPAN. Indeed, ether electrolytes have been considered to be incompatible with SPAN because of polysulfide shuttle problems.^[11b,e,13] For example, Archer and co-workers showed that the cells containing 1 M

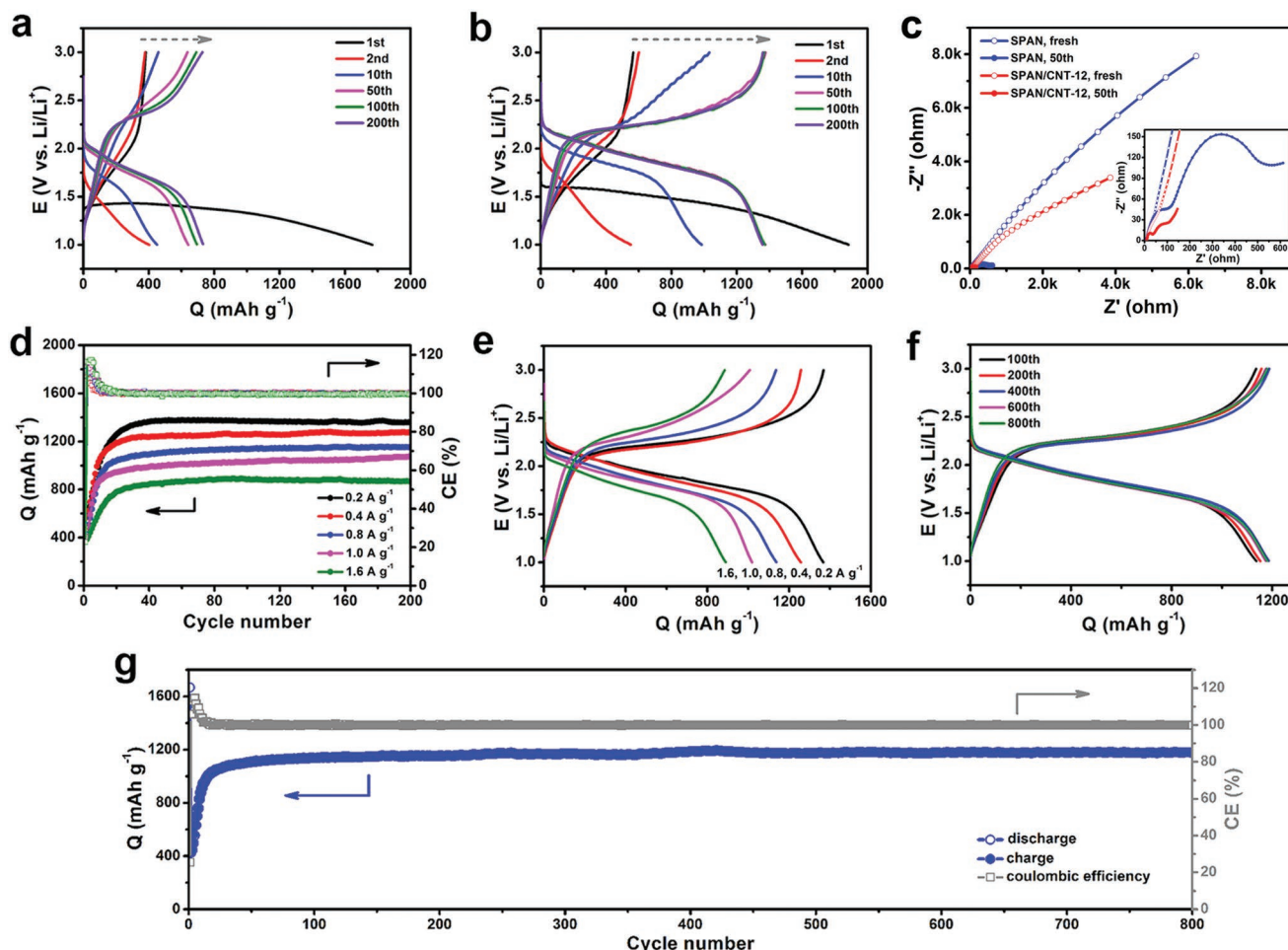


Figure 3. Electrochemical characteristics of SPAN and SPAN/CNT composites. The controlled electrolyte volume to active sulfur mass ratio (E/S) is $30 \mu\text{L mg}^{-1}$. a,b) Galvanostatic discharge–charge voltage profiles of SPAN and SPAN/CNT-12 at 200 mA g^{-1} . c) AC impedance spectra of SPAN and SPAN/CNT-12 electrodes. d) Rate capability of SPAN/CNT-12 electrode along with the respective Coulombic efficiency (CE) at different current densities. e) The discharge–charge profiles of the 100th cycle at different current densities. f) The representative discharge–charge profiles and g) the corresponding cyclic performance of SPAN/CNT-12 for longer-term operation at 800 mA g^{-1} .

LiTFSI–DOL/DME with/without LiNO_3 display poor cyclic stabilities.^[11e] The single one-step plateau on the first discharge profile excluded the presence of free S_8 in the pristine SPAN cathodes. However, a two-step discharge plateau was still observed from the second cycle, analogous to what has been seen in a conventional Li–S cell. Similar results were also reported.^[11b,13,21] The phenomenon was correlated with the electrochemical generation of free S_8 in the first recharge, resulting in a continuous diffusion of Li_2S_n in subsequent cycling. The unusual result was ascribed to the substantial high solubility of Li_2S_n in ether solvents, accelerating the spontaneous transformation of soluble intermediates. In ether electrolytes, S atoms that are not bonded to C but as long $-\text{S}_x-$ cross-links may easily release from the pyrolyzed PAN backbone, and then readily transform into high-order Li_2S_n and S_8 upon cell recharge. Therefore, most works cycled their SPAN electrodes in a mixture of carbonates despite the ether electrolytes have been proven as more compatible with metallic Li anodes.^[22] It seems that the bonding state of S plays a critical role in the cell chemistry.

The as-prepared electrodes should undergo through a solid-to-solid single-phase reaction, in which the SPAN, reduction intermediates (if any), and final product are insoluble. More evidence could be found in the zero self-discharge rate in ether electrolyte. The fully charged SPAN/CNT-12 electrode rested for 10, 20, and 30 d shows no capacity loss and 100% CE when getting recycled (Figure S9, Supporting Information). To demonstrate the compatibility of SPAN/CNT-12 electrode in carbonate-based electrolyte, a 1 M lithium hexafluorophosphate (LiPF_6) in a mixture of ethylene carbonate (EC), dimethyl carbonate (DMC), and ethyl methyl carbonate (EMC) (1/1/1, v/v) was used as a reference. In the galvanostatic and cyclic profiles (Figure S10a,b, Supporting Information), the capacity loss on the first cycle, subsequent steady-state voltage profiles, and single charge/discharge plateau are similar to those observed in ether electrolytes (Figure S10c, Supporting Information). The relatively lower capacity and higher voltage polarization are likely due to a higher internal resistance in carbonate electrolytes (Figure S10d, Supporting Information).

To understand the structure–property relationship, we calculated the electron structure of the experimentally proposed SPAN structures in Figure 2e by frontier molecular orbital (FMO) analysis. The optimized highest occupied molecular orbital (HOMO) and lowest unoccupied molecular orbital (LUMO) of structures ii and iii show the broken of S–S or C–S bonds, indicating a metastable state of these two structures (Figure S11, Supporting Information). The HOMO/LUMO electron structures of i and iv are stable with approximately the same energy levels and energy gap. We also calculated the reaction enthalpy by density functional theory (DFT) method to check the transformation to S₈ upon charge in the possible SPAN structures. Based on the reaction of PAN + S₈ → SPAN, the calculated reaction enthalpy (ΔH) for the structures of i, ii, iii, and iv is -0.29 , 0.20 , 0.08 , and -0.005 eV, respectively. A negative ΔH suggests the structures i and iv are thermodynamically unfavorable for S₈ formation with structure i being more rational. Combined with the electrochemical results, it is reasonable to demonstrate that structure i should be responsible for the absence of S₈ formation during the electrochemical processes.

2.4. Electrochemical Lithiation/Delithiation Processes of SPAN/CNT Nanofibers

The morphological evolution of SPAN/CNT-12 cathode at different discharge–charge states upon cycling, as marked in galvanostatic voltage profiles at 200 mA g⁻¹ (Figure 4a), was investigated by SEM. The SEM images of the pristine, 1st-discharged (1st-DC, 1.0 V), recharged (1st-RC, 3.0 V), 20th-discharged (20th-DC, 1.8 and 1.0 V), and recharged (20th-RC, 2.5 and 3.0 V) electrodes are shown in Figure 4b. The interconnected 3D nanofibrous network is well maintained through the continuous cyclic processes. However, distinguished from pristine nanofibers with clean surface (Figure 4b I), the 1st-DC nanofibers are covered thoroughly by uniform nanoflakes (Figure 4b II), which disappear after a recharge to 3.0 V with obvious deposits on the fibrous surface (Figure 4b III). The smoother nucleation, growth, and decomposition of the nanoflakes are more obvious after repeated activation cycles. Take the 20th cycle for instance, embryonic nanoflakes germinating on the nanofibers already exist when discharged to 1.8 V (Figure 4b IV) and the nanoflakes appear again at a full discharge to 1.0 V (Figure 4b V). In the subsequent recharge to 2.5 V, the nanoflakes transform to irregular-shaped deposits on the surface (Figure 4b VI), but a clean surface is observed when fully charged to 3.0 V (Figure 4b VII).

Additional spectroscopic measurements were carried out to further clarify the chemical composition of the nanoflakes, reduction/oxidation intermediates at various charge/discharge depth, the initial irreversible capacity loss, and structural evolution of SPAN during lithiation/delithiation. In consideration that it is hard to identify the sulfide species due to disproportional reactions and atmospheric contaminations, we adopted the organic conversation method by transferring S in SPAN into more stable benzylized polysulfide species (Bz₂S_x, $x \geq 1$) without changing the number of S atoms.^[11e,23] The Bz₂S_x could be analyzed via nuclear magnetic resonance spectrometry (¹H NMR) with nearly 100% conversation. A group of converted Bz₂S_x was

prepared by reacting a mixture of benzyl chloride (BzCl)/DME (1/1, v/v) with pristine, cycled SPAN/CNT-12 electrodes, and commercial Li₂S powders. The distinctive peaks in the region of 3.5–4.5 ppm would be identified as the methylene H of Bz₂S_x. As shown in Figure 5a, no characteristic NMR peaks of Bz₂S_x are identified from the pristine electrode, further proving that the entire S atoms are strongly bonded to the SPAN backbone. The 1st-DC electrode exhibits a single characteristic peak at 3.6 ppm, which is assigned to Bz₂S, in accordance with that of the Li₂S reference. The Raman spectrum of the 1st-DC electrode reveals the full cleavage of C–S and S–S bonds in SPAN molecule (Figure 5b), suggesting the full utilization of S. The reappearance of the C–S and S–S bonds in the Raman spectrum of the 1st-RC electrode suggests the reforming of SPAN. However, the NMR peak of Bz₂S shows the existence of residual Li₂S product in the 1st-RC electrode, which is supported by the low initial CE (30.1%). Assuming all S in SPAN converted into Li₂S, the capacity should be equal to theoretical capacity of S. However, the 1st-DC capacity (1884 mAh g⁻¹) exceeds the theoretical value. The origin of such an irreversible capacity loss on initial cycle was still in debates^[11e,13b,15,24] but a plausible explanation was the extra capacity contributed from the conjugated backbone.^[11b] The theoretical calculation by Jacob and co-workers suggested Li⁺ ions were preferentially coordinated with N atoms on the backbone, leading to strong adsorption energies.^[25] Recently, the poorly reversible reaction between Li⁺ and C=N backbone groups was verified by Yang and co-workers.^[11g] For clarification, a freestanding pyrolyzed PAN/CNT-12 (pPAN/CNT-12) electrode without sulfuration was synthesized as a control. It delivers an initial discharge capacity of 62 mAh g_{cathode}⁻¹ along with a sloped profile below 1.7 V (Figure S12a, Supporting Information). Only 11% of the capacity recovers in recharge and negligible capacity retains in following cycles (Figure S12b, Supporting Information). In voltage window of 1–3 V, any Li-intercalated graphite as charge carrier can be ruled out since such a system would start discharging at 0.1–0.2 V. The low CE of pPAN/CNT-12 is very likely to arise from the backbone groups. Therefore, the Li⁺ reaction with SPAN backbone, probably with C=N to form Li–C–N–Li, contributes to the over-discharge capacity in the initial cycle, and the dissociation of Li⁺ from the backbone is almost irreversible.

The residual Li⁺ in the backbone should be helpful for the activation of Li₂S, because the reversible capacity is gradually increased and the charge/discharge hysteresis is gradually decreased. For example, the discharge capacity on the second and tenth cycle is 552 and 986 mAh g⁻¹ with a respective recharge capacity of 601 and 1032 mAh g⁻¹. A vial type Li–S cell assembled with SPAN/CNT-12 cathode and Li-metal anode immersed in 5 mL ether electrolyte was used to confirm that there are no soluble polysulfides formed upon cycling. As shown in the digital images (Figure S13, Supporting Information), the color of electrolyte keeps transparent during the first cycle, suggesting the absence of soluble polysulfides that are typically brownish red in electrolyte.^[26] XRD analysis was used to study the crystalline structural evolution of electrode during cycling. Figure S14 (Supporting Information) shows the ex situ XRD patterns of the pristine SPAN/CNT-12 electrode and the electrodes after 1st-DC and 1st-RC SPAN/CNT-12 with commercial sulfur (S₈) and Li₂S as references. The cycled electrodes

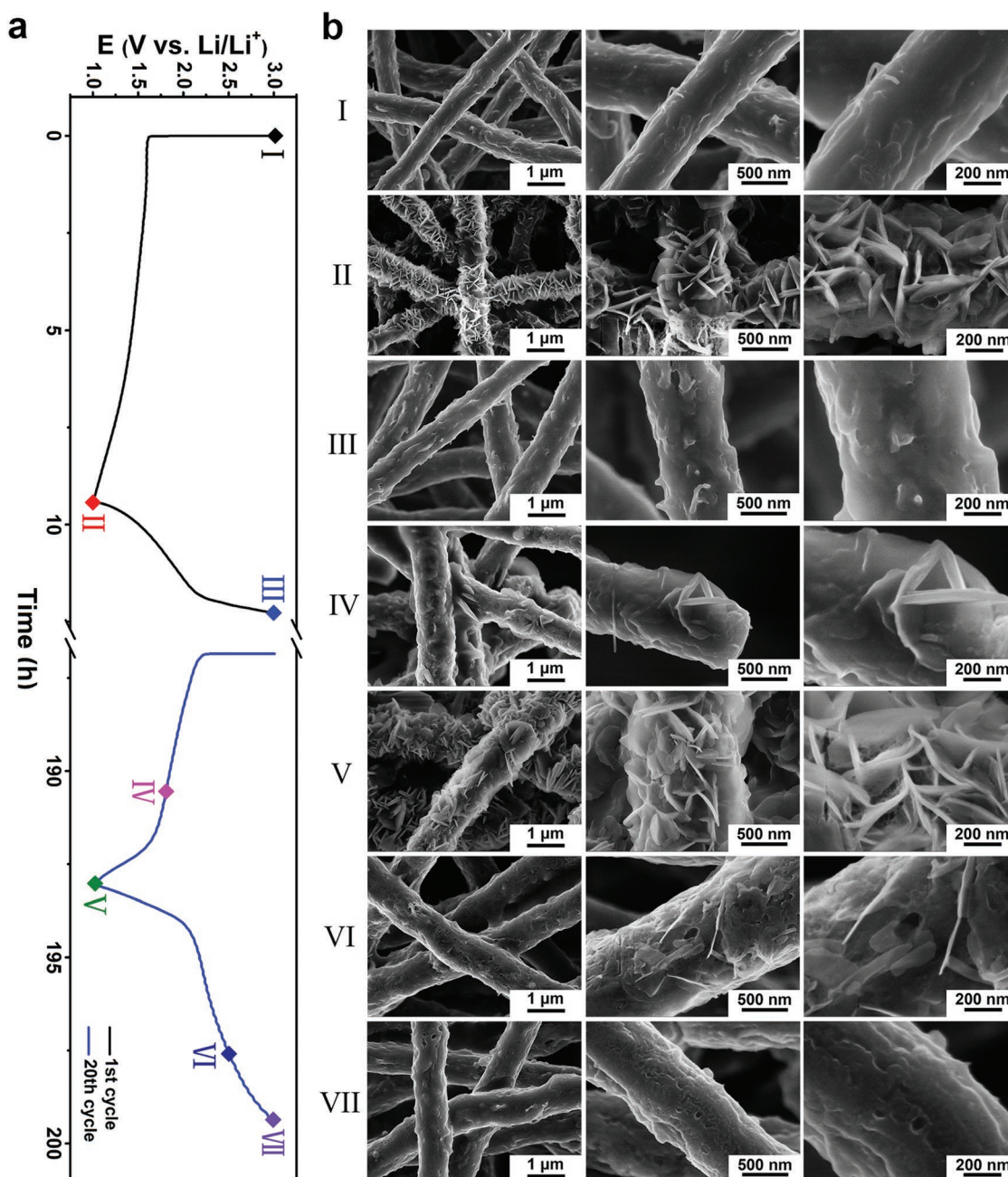


Figure 4. a) The discharge–charge profiles of the 1st and 20th operation cycle. Sampling points for characterizations were marked with corresponding colored dots and numbers. b) SEM images of SPAN/CNT-12 electrodes at (I) pristine state, (II) 1st-discharged to 1.0 V (1st-DC, 1.0 V), (III) 1st-recharged to 3.0 V (1st-RC, 3.0 V), (IV) 20th-discharged to 1.8 V (20th-DC, 1.8 V), (V) 20th-discharged to 1.0 V (20th-DC, 1.0 V), (VI) 20th-recharged to 2.5 V (20th-RC, 2.5 V), and (VII) 20th-recharged to 3.0 V (20th-RC, 3.0 V).

were extensively washed to remove the lithium salts. In addition to the characteristic peak of graphitized PAN, the 1st-DC electrode shows pronounced peaks that can be assigned to the characteristic diffraction peaks of Li_2S . These peaks are still visible with a decreased intensity in the electrode after 1st-RC. No peaks ascribed to other polysulfides or S_8 are detected. In NMR spectra of the 20th-DC electrodes, the peak assigned to Li_2S appears irrespective depth of discharge. Except for Li_2S , there are no signals of intermediates when discharging to 1.8 V or

recharging to 2.5 V. UV–vis absorption spectra recorded on the solution collected by extensively washing the cycled electrodes at intermediate stage further prove the absence of soluble Li_2S_n intermediates (Figure S15, Supporting Information). The nanoflakes on nanofibers can be identified as Li_2S , the predominant product and the only sulfide product of SPAN. Raman spectra of the 20th-DC and 20th-RC electrodes at various stages further prove the reversible cleavage and recombination of C–S and S–S bonds in SPAN. Although the weak signal of Li_2S is still

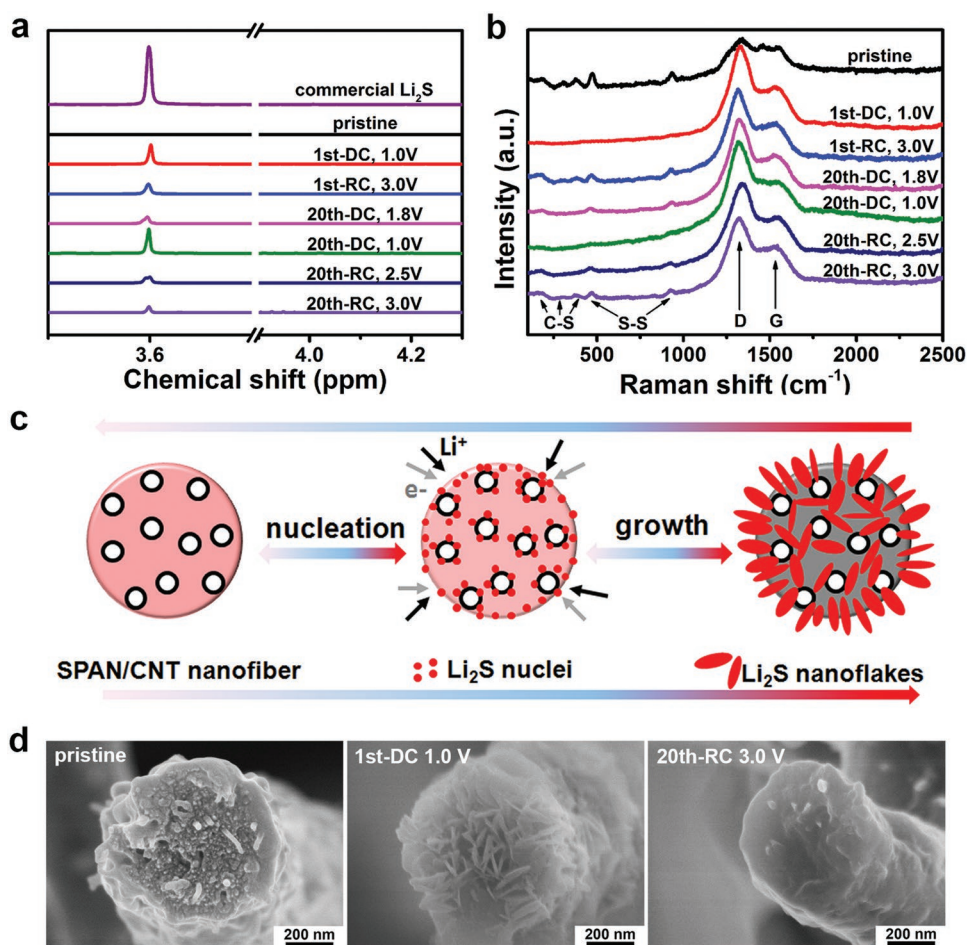


Figure 5. a) ^1H NMR spectra of the converted Bz_2S_x ($x \geq 1$) from commercial Li_2S powder, SPAN/CNT-12 electrode at pristine and various states of discharge–charge. b) Raman spectra in the range of $100\text{--}2500\text{ cm}^{-1}$ of SPAN/CNT-12 electrode at pristine and various states of discharge–charge. c) Schematic illustration for the nucleation–growth/decomposition of Li_2S nanoflakes from the cross-sectional view of the SPAN/CNT-12 nanofibers. d) Cross-sectional SEM images of a single SPAN/CNT-12 nanofiber at different discharge–charge states.

detectable in the NMR spectrum from the fully charged electrode at the 20th cycle, the high reversible capacity suggests a highly reversible manner of Li_2S production/decomposition.

Based on the above observations, the electrochemical processes mainly involve the nucleation–growth/decomposition of Li_2S nanoflakes, as schematically presented in Figure 5c. Li_2S is expected to nucleate on the surface of nanofibers and CNTs at initial discharge. With the continuous reduction of S, Li_2S nuclei form throughout the nanofibers and grow into nanoflakes. The decomposition of Li_2S is in a fully reversible manner and does not destroy the nanofibrous SPAN (Figure 5d). The corresponding overall electrochemical lithiation/delithiation process is proposed in Figure 6a. During the first discharge, the cleavage of S–S and then C–S linkages (more explanation can be found in Figure S16, Supporting Information) lead to the formation of Li_2S . Because of the unique $-\text{S}_x-$ structure with $x \leq 3$ in SPAN, the entire S is solely transformed into Li_2S without the formation of sulfide intermediates. Meanwhile, partial C=N bonds break and react with Li^+ to form $\text{Li}-\text{C}-\text{N}-\text{Li}$. The discharge products are in fact a mixture of the Li coordinated polymer backbone (denoted as PAN-Li) and Li_2S , but

PAN-Li almost cannot proceed the delithiation reaction on the first recharge, leading to the presence of residual Li in the sulfurized polymer backbone (denoted as SPAN-Li). After the first discharge, the reversible redox reaction takes place between SPAN-Li and Li_2S .

We analyzed the electron structure of the polymer backbone during the charge/discharge process by FMO analysis. Figure 6b shows the calculated HOMO/LUMO energy gap of SPAN, SPAN-Li, and PAN-Li. The LUMOs of SPAN and SPAN-Li mainly distribute around the backbones, indicating the backbones serve as the electron acceptor during the discharge process. The HOMOs of SPAN-Li and PAN-Li mainly distribute around the S atoms and backbones, respectively, which serve as the electron donor during the charge process. According to the FMO theory, good conductivity of a molecule is attributed to small gaps between energy levels.^[27] The energy gap gradually decreases from 1.92 eV for SPAN to 1.15 eV for SPAN-Li and finally to 0.5 eV for PAN-Li, suggesting enhanced conductivity. Such a phenomenon is in good agreement to the experimental results: The lithiation of SPAN makes the polymer backbone more conductive, and the removal of S atom from the lithiated

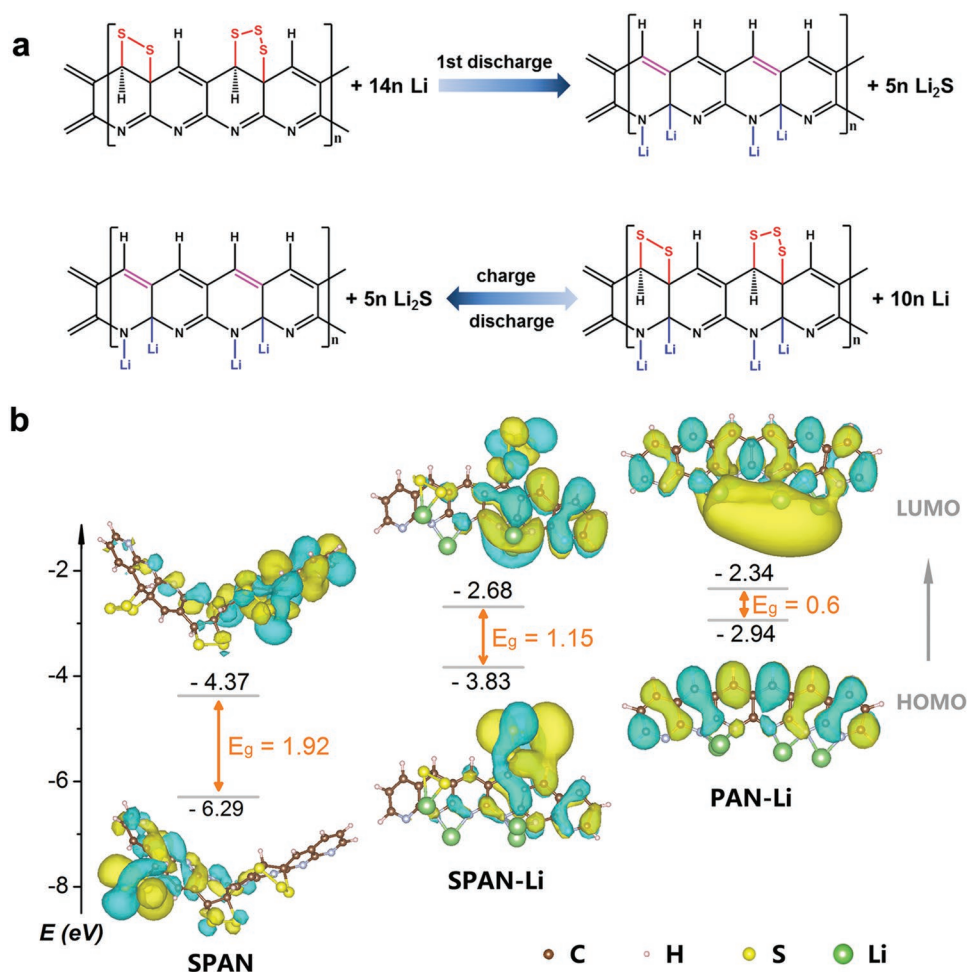


Figure 6. a) The proposed overall electrochemical lithiation/delithiation processes of as-prepared SPAN. b) The calculated HOMO/LUMO energy level diagrams of SPAN, partially lithiated SPAN (SPAN-Li), and fully lithiated PAN (PAN-Li) by frontier molecular orbital analysis. E_g is the energy gap between HOMO and LUMO.

SPAN further enhances its conductivity. Theoretically, a 100% reversible production/decomposition of Li_2S could be achieved accompanying with the reversible cleaving/reforming of S–S and C–S bonds in SPAN.

3. Conclusions

In summary, a freestanding SPAN/CNT electrode was prepared by a straightforward tactics combining the electrospinning technique and heat treatment. The interwoven network of pyrolyzed SPAN/CNT nanofiber not only accelerates charge transfer but also supplies quick ionic transport channels. More importantly, the strongly bonded S in the form of short $-\text{S}_2-$ and $-\text{S}_3-$ in SPAN enables its compatibility in both ether and carbonate electrolytes. The nucleation–growth/decomposition of Li_2S nanoflakes on PAN-derived nanofibers is clearly observed for the first time. The reaction kinetics between SPAN and Li^+ is controlled by the activation energy of Li_2S product. The control of Li_2S formation and the improvement on interfacial charge transfer between the polymer frameworks and Li_2S crystals hold the promise to further boost the performance of SPAN cathodes.

4. Experimental Section

Synthesis of PAN/CNT Precursor Nanofibers: The PAN/CNT precursor nanofibers were prepared via an electrospinning method. First, CNTs (multiwalled, 98% purity, diameter (d) = 10–20 nm) were acid-leached with a mixture of $\text{H}_2\text{SO}_4/\text{HNO}_3$ (1/1, v/v) at 70 °C for 1 h, washed with deionized water thoroughly and dried before use. Then, 40, 80, 120, and 160 mg of CNTs were dispersed in 9 g DMF (99.5%, Shanghai Lingfeng Chemical), respectively. After sonication for 45 min, 1 g PAN ($M_w = 15\,000$, Sigma-Aldrich) was dissolved in each of the solution under vigorous stirring for 12 h. Finally, the homogeneous mixed solutions were inhaled into a syringe (10 mL) with a stainless-steel needle and spun by applying a work voltage of 18 kV. The feeding rate and gap between the needle and collector were fixed at 0.1 mm min^{-1} (1.6 mL h^{-1} in volume/time) and 24 cm. After electrospinning, flexible and freestanding PAN/CNT films with different CNT contents were obtained. Because the mass ratio of CNTs to PAN is 4, 8, 12, and 16 wt%, these samples are denoted as PAN/CNT-4, PAN/CNT-8, PAN/CNT-12, and PAN/CNT-16, respectively. In addition, a controlled CNT-free sample denoted as PAN was prepared at the same condition.

Synthesis of SPAN/CNT Nanofibers: The PAN/CNT precursor films were put onto a layer of sublimed sulfur (chemical purity, Sinopharm Chemical) and heated in a tube furnace at 350 °C for 3 h with a ramping rate of $5 \text{ }^\circ\text{C min}^{-1}$ under a flowing nitrogen atmosphere. To ensure the obtained SPAN/CNT electrode with a saturated sulfur content, slightly

excessive sublimed sulfur should be used. The as-prepared flexible and freestanding SPAN cathodes with various amounts of CNTs are designated as SPAN/CNT-4, SPAN/CNT-8, SPAN/CNT-12, and SPAN/CNT-16, respectively. The CNT-free one is marked as SPAN.

Material Characterizations: The morphology and microstructure of the samples were characterized by FESEM (S-4800, HITACHI) and TEM (JEM-2100F, JEOL) combined with EDS. To detect the crystallinity, XRD patterns were employed using an X-ray diffractometer (D/max-2550VB+/PC, Rigaku) equipped with Cu K α radiation. Raman spectra were collected by an inVia Reflex Raman Spectrometer (inVia-Reflex, Renishaw). For FTIR measurements, the dried films were ground and pressed with KBr powders (99%, Sigma-Aldrich) to make pellets and recorded on a FTIR spectrometer (Bruker VECTOR22). UV-vis spectra were recorded by using a UV-vis spectrophotometer (Lambda-35). XPS analyses were performed by using a spectrometer (Escalab 250Xi) with Al K α X-ray radiation. The thermal stability was assessed by TGA (NETZSCH TG 209 F1 Libra) in the temperature range from ambient to 1000 °C in N₂. Element content analysis was measured by elemental analyzer (Vario EL III, Elementar, Germany).

For SEM, Raman, and XRD analyses on electrodes evaluated at different states of discharge-charge, the electrodes were washed by DME and dried in the glove box overnight before use. The ¹H NMR was conducted on a Varian 600 MHz spectrometer at ambient temperature. To convert the sulfur species in SPAN/CNT-12 into Bz₂S_x ($x \geq 1$),^[11e,23] the pristine and cycled electrodes were immersed in the mixture of BzCl/DME (1/1, v/v) and sonicated for 1 h. The cycled electrodes for ¹H NMR analysis were not washed to preserve all the products. Each sample was then allowed to sit for 4 d to be completely converted. After the solvent was evaporated, the samples were then mixed with chloroform-d and filtered out of polymer matrix. Finally, the filtrate was used for ¹H NMR analysis. As a control, commercial Li₂S powder was added to the mixture of BzCl/DME in the same manner and tested by ¹H NMR.

Electrochemical Measurements: For electrochemical tests, SPAN and SPAN/CNT films with a typical thickness of $\approx 40 \mu\text{m}$ were punched into discs with a diameter of 12 mm. If not specially mentioned, the average S loading is $\approx 2.0 \text{ mg cm}^{-2}$. The freestanding discs were used as electrodes directly without additional carbons or binders in CR2025 type coin cells. A current collector was also not used. The cells were assembled in an argon-filled glove box (<1 ppm of H₂O and O₂, Mikrouna) with a separator of polypropylene/polypropylene microporous membrane (Celgard 2325). If not specially mentioned, 1 M of LiTFSI in DOL/DME (1/1, v/v) in presence of 0.2 M of LiNO₃ was used as electrolyte. For comparison, 1 M LiPF₆-EC/DMC/EMC (1/1/1, v/v) was tested as an alternative. The galvanostatic tests were performed on a LAND battery test system (Wuhan, China) at room temperature of 25 °C upon various current densities in a voltage window of 1.0–3.0 V. CV measurements were carried out by an electrochemical workstation (Arbin Instruments, USA) between 1.0 and 3.0 V. Electrochemical impedance spectroscopy (EIS) measurements were conducted on a CHI660E electrochemical workstation in a frequency range from 0.1 Hz to 100 kHz.

Calculation Method: Electron configurations of all the molecules were calculated by DFT method within the framework of the Gaussian 09 package.^[28] The standard Pople basis set, 6-311G(d,p) combined with the Lee–Yang–Parr exchange correlation functional (B3LYP)^[29] was used for all calculations. For each molecule, the geometry was fully optimized to achieve the lowest total energy before energy level calculation, and all possible spin multiplicities were explored ($S = 0, 1, 2$), among which the one with the lowest energy was chosen for comparison between different molecules.

Supporting Information

Supporting Information is available from the Wiley Online Library or from the author.

Acknowledgements

The authors acknowledge funding support from the National Natural Science Foundation of China (21603030 and 51433001), the Natural Science Foundation of Shanghai (17ZR1446400), the Fundamental Research Funds for the Central Universities (2232018D3-02), the Program of Shanghai Academic Research Leader (17XD1400100), and the Shanghai Scientific and Technological Innovation Project (18JC1410600).

Conflict of Interest

The authors declare no conflict of interest.

Keywords

electrolyte, lithium sulfide, lithium–sulfur battery, reaction mechanism, sulfurized polyacrylonitrile

Received: April 11, 2019

Revised: July 3, 2019

Published online:

- [1] a) P. G. Bruce, S. A. Freunberger, L. J. Hardwick, J.-M. Tarascon, *Nat. Mater.* **2012**, *11*, 19; b) A. Manthiram, S.-H. Chung, C. Zu, *Adv. Mater.* **2015**, *27*, 1980.
- [2] a) N.-S. Choi, Z. Chen, S. A. Freunberger, X. Ji, Y.-K. Sun, K. Amine, G. Yushin, L. F. Nazar, J. Cho, P. G. Bruce, *Angew. Chem. Int. Ed.* **2012**, *51*, 9994; b) L. Wang, J. Liu, S. Yuan, Y. Wang, Y. Xia, *Energy Environ. Sci.* **2016**, *9*, 224.
- [3] L. Wang, Y. Zhao, M. L. Thomas, H. R. Byon, *Adv. Funct. Mater.* **2014**, *24*, 2248.
- [4] J. Wang, C. Fu, X. Wang, Y. Yao, M. Sun, L. Wang, T. Liu, *Electrochim. Acta* **2018**, *292*, 568.
- [5] H. Wang, Y. Yang, Y. Liang, J. T. Robinson, Y. Li, A. Jackson, Y. Cu, H. Dai, *Nano Lett.* **2011**, *11*, 2644.
- [6] a) X. Ji, K. T. Lee, L. F. Nazar, *Nat. Mater.* **2009**, *8*, 500; b) J. Zhang, C.-P. Yang, Y.-X. Yin, L.-J. Wan, Y.-G. Guo, *Adv. Mater.* **2016**, *28*, 9539; c) Y. Zhong, X. Xia, S. Deng, J. Zhan, R. Fang, Y. Xia, X. Wang, Q. Zhang, J. Tu, *Adv. Energy Mater.* **2018**, *8*, 1701110.
- [7] a) Z. Li, J. Zhang, X. W. Lou, *Angew. Chem. Int. Ed.* **2015**, *54*, 12886; b) M. Yu, J. Ma, H. Song, A. Wang, F. Tian, Y. Wang, H. Qiu, R. Wang, *Energy Environ. Sci.* **2016**, *9*, 1495; c) L. Hu, C. Dai, H. Liu, Y. Li, B. Shen, Y. Chen, S.-J. Bao, M. Xu, *Adv. Energy Mater.* **2018**, *8*, 1800709.
- [8] a) L. Ma, S. Wei, H. L. Zhuang, K. E. Hendrickson, R. G. Hennig, L. A. Archer, *J. Mater. Chem. A* **2015**, *3*, 19857; b) X. Zhu, W. Zhao, Y. Song, Q. Li, F. Ding, J. Sun, L. Zhang, Z. Liu, *Adv. Energy Mater.* **2018**, *8*, 1800201.
- [9] S. Xin, L. Gu, N.-H. Zhao, Y.-X. Yin, L.-J. Zhou, Y.-G. Guo, L.-J. Wan, *J. Am. Chem. Soc.* **2012**, *134*, 18510.
- [10] a) J. Wang, J. Xie, N. Xu, *Adv. Mater.* **2002**, *14*, 963; b) J. Wang, J. Yang, C. Wan, K. Du, J. Xie, N. Xu, *Adv. Funct. Mater.* **2003**, *13*, 487.
- [11] a) X. Yu, J. Xie, J. Yang, H. Huang, K. Wang, Z. Wen, *J. Electroanal. Chem.* **2004**, *573*, 121; b) J. Fanous, M. Wegner, J. Grimming, Å. Andresen, M. R. Buchmeiser, *Chem. Mater.* **2011**, *23*, 5024; c) J. Fanous, M. Wegner, J. Grimming, M. Rolff, M. B. M. Spera, M. Tenzer, M. R. Buchmeiser, *J. Mater. Chem.* **2012**, *22*, 23240; d) T. H. Hwang, D. S. Jung, J.-S. Kim, B. G. Kim, J. W. Choi, *Nano*

- Lett.* **2013**, *13*, 4532; e) S. Wei, L. Ma, K. E. Hendrickson, Z. Tu, L. A. Archer, *J. Am. Chem. Soc.* **2015**, *137*, 12143; f) M. Frey, R. K. Zenn, S. Warneke, K. Müller, A. Hintennach, R. E. Dinnebie, M. R. Buchmeiser, *ACS Energy Lett.* **2017**, *2*, 595; g) Z.-Q. Jin, Y.-G. Liu, W.-K. Wang, A.-B. Wang, B.-W. Hu, M. Shen, T. Gao, P.-C. Zhao, Y.-S. Yang, *Energy Storage Mater.* **2018**, *14*, 272; h) W. Wang, Z. Cao, G. A. Elia, Y. Wu, W. Wahyudi, E. Abou-Hamad, A.-H. Emwas, L. Cavallo, L.-J. Li, J. Ming, *ACS Energy Lett.* **2018**, *3*, 2899.
- [12] a) S. S. Zhang, *J. Power Sources* **2013**, *231*, 153; b) T. Yim, M.-S. Park, J.-S. Yu, K. J. Kim, K. Y. Im, J.-H. Kim, G. Jeong, Y. N. Jo, S.-G. Woo, K. S. Kang, I. Lee, Y.-J. Kim, *Electrochim. Acta* **2013**, *107*, 454.
- [13] a) L. Wang, X. He, J. Li, M. Chen, J. Gao, C. Jiang, *Electrochim. Acta* **2012**, *72*, 114; b) S. S. Zhang, *Energies* **2014**, *7*, 4588; c) S. Warneke, M. Eusterholz, R. K. Zenn, A. Hintennach, R. E. Dinnebie, M. R. Buchmeiser, *J. Electrochem. Soc.* **2018**, *165*, A6017.
- [14] J. Ye, F. He, J. Nie, Y. Cao, H. Yang, X. Ai, *J. Mater. Chem. A* **2015**, *3*, 7406.
- [15] L. Yin, J. Wang, F. Lin, J. Yang, Y. Nuli, *Energy Environ. Sci.* **2012**, *5*, 6966.
- [16] a) X. Yu, J. Xie, Y. Li, H. Huang, C. Lai, K. Wang, *J. Power Sources* **2005**, *146*, 335; b) H. M. Kim, J.-Y. Hwang, D. Aurbach, Y.-K. Sun, *J. Phys. Chem. Lett.* **2017**, *8*, 5331.
- [17] J. Riga, J. J. Verbist, *J. Chem. Soc., Perkin Trans. 2* **1983**, 1545.
- [18] J. Guo, Z. Wen, Q. Wang, J. Jin, G. Ma, *J. Mater. Chem. A* **2015**, *3*, 19815.
- [19] Y. Li, Q. Zeng, I. R. Gentle, D.-W. Wang, *J. Mater. Chem. A* **2017**, *5*, 5460.
- [20] a) L. Qie, A. Manthiram, *Adv. Mater.* **2015**, *27*, 1694; b) M. Yu, Z. Wang, Y. Wang, Y. Dong, J. Qiu, *Adv. Energy Mater.* **2017**, *7*, 1700018.
- [21] S. Warneke, R. K. Zenn, T. Leberher, K. Müller, A. Hintennach, U. Starke, R. E. Dinnebie, M. R. Buchmeiser, *Adv. Sustainable Syst.* **2018**, *2*, 1700144.
- [22] a) J. Qian, W. A. Henderson, W. Xu, P. Bhattacharya, M. Engelhard, O. Borodin, J.-G. Zhang, *Nat. Commun.* **2015**, *6*, 6362; b) T.-T. Zuo, X.-W. Wu, C.-P. Yang, Y.-X. Yin, H. Ye, N.-W. Li, Y.-G. Guo, *Adv. Mater.* **2017**, *29*, 1700389.
- [23] A. Kawase, S. Shirai, Y. Yamoto, R. Arakawac, T. Takatad, *Phys. Chem. Chem. Phys.* **2014**, *16*, 9344.
- [24] a) J. Li, K. Li, M. Li, D. Gosselink, Y. Zhang, P. Chen, *J. Power Sources* **2014**, *252*, 107; b) H. Chen, C. Wang, C. Hu, J. Zhang, S. Gao, W. Lu, L. Chen, *J. Mater. Chem. A* **2015**, *3*, 1392; c) Y. Liu, A. K. Haridas, K.-K. Cho, Y. Lee, J.-H. Ahn, *J. Phys. Chem. C* **2017**, *121*, 26172.
- [25] T. Zhu, J. E. Mueller, M. Hanauer, U. Sauter, T. Jacob, *ChemElectroChem* **2017**, *4*, 2975.
- [26] a) X. Liang, C. Hart, Q. Pang, A. Garsuch, T. Weiss, L. F. Nazar, *Nat. Commun.* **2015**, *6*, 5682; b) Z.-Z. Yang, H.-Y. Wang, L. Lu, C. Wang, X.-B. Zhong, J.-G. Wang, Q.-C. Jiang, *Sci. Rep.* **2016**, *6*, 22990.
- [27] Y. Tsuji, R. Hoffmann, *Angew. Chem. Int. Ed.* **2014**, *53*, 4093.
- [28] M. J. Frisch, G. W. Trucks, H. B. Schlegel, G. E. Scuseria, M. A. Robb, J. R. Cheeseman, G. Scalmani, V. Barone, B. Mennucci, G. A. Petersson, H. Nakatsuji, M. Caricato, X. Li, H. P. Hratchian, A. F. Izmaylov, J. Bloino, G. Zheng, J. L. Sonnenberg, M. Hada, M. Ehara, K. Toyota, R. Fukuda, J. Hasegawa, M. Ishida, T. Nakajima, Y. Honda, O. Kitao, H. Nakai, T. Vreven, J. A. Montgomery Jr., J. E. Peralta, F. Ogliaro, M. Bearpark, J. J. Heyd, E. Brothers, K. N. Kudin, V. N. Staroverov, R. Kobayashi, J. Normand, K. Raghavachari, A. Rendell, J. C. Burant, S. S. Iyengar, J. Tomasi, M. Cossi, N. Rega, J. M. Millam, M. Klene, J. E. Knox, J. B. Cross, V. Bakken, C. Adamo, J. Jaramillo, R. Gomperts, R. E. Stratmann, O. Yazyev, A. J. Austin, R. Cammi, C. Pomelli, J. W. Ochterski, R. L. Martin, K. Morokuma, V. G. Zakrzewski, G. A. Voth, P. Salvador, J. J. Dannenberg, S. Dapprich, A. D. Daniels, Ö. Farkas, J. B. Foresman, J. V. Ortiz, J. Cioslowski, D. J. Fox, Gaussian 09, Revision D.01, Gaussian Inc., Wallingford, CT **2009**.
- [29] A. D. Becke, *J. Chem. Phys.* **1993**, *98*, 5648.